


RESEARCH ARTICLE

Magnetic Resonance in Medicine

B1-MRF: Large dynamic range MRF-based absolute B_1^+ mapping in the human body at 7T

Max Lutz¹  | Christoph Stefan Aigner¹  | Sebastian Flassbeck^{2,3}  | Felix Krueger¹  |
Constance G. F. Gatefait¹ | Christoph Kolbitsch¹  | Berk Silemek¹  | Frank Seifert¹  |
Tobias Schaeffter^{1,4,5} | Sebastian Schmitter^{1,6,7} 

¹Physikalisch-Technische Bundesanstalt, Braunschweig and Berlin, Germany

²Bernard and Irene Schwartz Center for Biomedical Imaging, Department of Radiology, New York University Grossman School of Medicine, New York, New York, USA

³Center for Advanced Imaging Innovation and Research (CAI²R), Department of Radiology, New York University Grossman School of Medicine, New York, New York, USA

⁴Einstein Center Digital Future, Berlin, Germany

⁵Department of Biomedical Engineering, Technical University of Berlin, Berlin, Germany

⁶Center for Magnetic Resonance Research, University of Minnesota, Minneapolis, Minnesota, USA

⁷Medical Physics in Radiology, German Cancer Research Center (DKFZ), Heidelberg, Germany

Correspondence

Max Lutz, Physikalisch-Technische Bundesanstalt, Biomedical Magnetic Resonance – 8.1, Abbestr. 2-12, 10587 Berlin, Germany.
Email: max.lutz@ptb.de

Funding information

German Research Foundation, Grant/Award Numbers: SCHM 2677/4-1, GRK2260

Abstract

Purpose: This study aims to map the transmit magnetic field (B_1^+) in the human body at 7T using MR fingerprinting (MRF), with a focus on achieving high accuracy and precision across a large dynamic range, particularly at low flip angles (FAs).

Methods: A FLASH-based MRF sequence (B1-MRF) with high B_1^+ sensitivity was developed. Phantom and in vivo abdominal imaging were performed at 7T, and the results were compared with established reference methods, including a slow but precise preparation-based method (PEX), saturated TurboFLASH (satTFL), actual flip angle imaging (AFI) and Bloch-Siegert shift (BSS).

Results: The MRF signal curve was highly sensitive to B_1^+ , while T_1 sensitivity was comparatively low. The phantom experiment showed good agreement of B_1^+ to PEX for a T_1 range of 204–1691 ms evaluated at FAs from 0° to 70°. Compared to the references, a dynamic range increase larger than a factor of two was determined experimentally. In vivo liver scans showed a strong correlation between B1-MRF, satTFL, and RPE-AFI in a low body mass index (BMI) subject (18.1 kg/m²). However, in larger BMI subjects (≥ 25.5 kg/m²), inconsistencies were observed in low B_1^+ regions for satTFL and RPE-AFI, while B1-MRF still provided consistent results in these regions.

Conclusion: B1-MRF provides accurate and precise B_1^+ maps over a wide range of FAs, surpassing the capabilities of existing methods in the FA range < 60°. Its enhanced sensitivity at low FAs is advantageous for various applications requiring precise B_1^+ estimates, potentially advancing the frontiers of ultra-high field (UHF) body imaging at 7T and beyond.

KEYWORDS

7 Tesla, B_1^+ mapping, body MRI, MRF, ultrahigh field MRI

Parts of this work have been presented at the 2022 Annual Meeting of the International Society for Magnetic Resonance in Medicine.

This is an open access article under the terms of the [Creative Commons Attribution](https://creativecommons.org/licenses/by/4.0/) License, which permits use, distribution and reproduction in any medium, provided the original work is properly cited.

© 2024 Physikalisch-Technische Bundesanstalt (PTB) and The Author(s). *Magnetic Resonance in Medicine* published by Wiley Periodicals LLC on behalf of International Society for Magnetic Resonance in Medicine.

1 | INTRODUCTION

Accurate and precise mapping of the transmit magnetic field (B_1^+) is essential for several MRI applications, including quantitative correction,^{1,2} safety validation,³ and parallel transmission (pTx).^{4,5} At ultra-high fields (UHF) of 7T and above, the B_1^+ -field experiences constructive and destructive RF interference due to the reduced wavelength, resulting from an increased Larmor frequency. When targeting a large FOV, such as the human abdomen, a strong variability in B_1^+ amplitude is observed, ranging from regions of high B_1^+ amplitude to regions of low amplitude or even “drop-out areas.”^{6–8} Mapping the B_1^+ -field in the human abdomen over this large dynamic range is challenging.

Several techniques, including actual flip angle imaging (AFI),⁹ saturated TurboFLASH (satTFL),¹⁰ dual refocusing echo acquisition (DREAM),¹¹ and Bloch-Siegert shift (BSS),¹² have been developed for absolute B_1^+ -field mapping and have been applied at UHF. While these methods provide accurate B_1^+ -maps within a limited dynamic B_1^+ range for regions such as the human head,¹³ challenges arise in other areas, such as the abdomen. These challenges include RF power limitations, reduced efficiency of the transmit coils compared to the head, specific absorption rate (SAR) constraints, physiological motion, and larger FOVs resulting in extended acquisition times unsuitable for breath-hold protocols.^{13–15} Moreover, the dynamic range of these techniques is limited due to a decreased accuracy at flip angles (FAs) below 20°. ^{13,14} Decreased accuracy at low FAs is an issue for precise B_1^+ mapping in the body at UHF, as increasing FAs to improve sensitivity is limited by RF power and SAR constraints.

An approach capable of encoding B_1^+ , among other parameters of interest, is MR fingerprinting (MRF).¹⁶ MRF is a quantitative MRI technique in which acquisition parameters (e.g., FA/TR) are varied to produce a specific signal response depending on the tissue properties of the scanned sample as well as the magnetic fields applied to obtain MRI signals. High undersampling factors are typically used, and the resulting signals are matched to simulations. In prior MRF studies, two approaches have emerged for estimating B_1^+ to correct for its effect on relaxation parameters: (1) A separate B_1^+ mapping scan is performed, and its values are then included in the fingerprint simulations.^{17,18} This requires additional scan time, and noise from B_1^+ -maps may propagate to the quantitative parameter maps.^{19,20} (2) B_1^+ is included as a dimension in the fingerprint simulations,^{19,21–25} eliminating the need for an additional scan. However, then the MRF sequence must be designed to be B_1^+ sensitive.

The second approach allows direct quantification of B_1^+ using the MRF framework and has been validated by

several studies where the main goal was an accurate estimation of relaxation parameters: Buonincontri and Sawiak's SSFP-based MRF sequence with abrupt FA changes at 4.7T²¹ showed a 4.0% difference from the double angle method²⁶ for sinc pulses in a range of 0.5–1.5 times the nominal FA in a rat brain. When adapted for human head imaging at 7T,²² this method aligned well qualitatively with BSS¹² for a phantom, although no quantitative values were provided. Körzdörfer et al.²³ integrated SSFP, FISP, and FLASH segments in a sequence for head and abdominal imaging at 3T, yielding good B_1^+ agreement with a vendor-provided method²⁷ over a range of 0.8–1.2 times the nominal FA.

Cloos et al.¹⁹ introduced the Plug-and-Play MRF sequence, combining FISP and FLASH with two B_1^+ shims, which circumvents extensive B_1^+ calibration at UHF. This method showed good agreement with satTFL¹⁰ for phantoms at 3T in the range of $\sim 2.5 \mu\text{T}$ – $6.5 \mu\text{T}$. Van Riel et al.²⁵ used a 3D radial-stack-of-stars FLASH sequence for abdominal imaging at 3T, demonstrating good B_1^+ agreement with satTFL¹⁰ in the range of $0.04 \mu\text{T/V}$ – $0.06 \mu\text{T/V}$ for a phantom. Cloos et al.²⁴ further adapted the Plug-and-Play MRF sequence for in vivo abdominal T_1 and B_1^+ mapping at 7T, but a comparative reference B_1^+ -map was not provided in their preliminary study.

The aforementioned works indicate that MRF is a highly promising technique for accurate B_1^+ mapping. However, there is currently no comprehensive study investigating the accuracy and precision and the dynamic range of mapping B_1^+ using MRF and comparing it with reference methods in the body at 7T.

Therefore, the aim of this work is to fill this knowledge gap and to develop and evaluate an MRF sequence for accurate and precise mapping of B_1^+ over a large dynamic range, termed B1-MRF. In contrast to previous MRF approaches, the goal of our work is to achieve accurate B_1^+ estimation through high B_1^+ sensitivity, while sensitivity to T_1 and T_2 should be low. To achieve this, we use a FLASH sequence without preparation pulses that includes B_1^+ , T_1 , and only coarse T_2 in the MRF dictionary. The dynamic B_1^+ range is evaluated by considering the sensitivity of the MRF signal to B_1^+ and performing phantom experiments over a wide B_1^+ range. Comparison of B1-MRF with satTFL and AFI during a 7T abdominal scan shows better consistency in low FA regions for B1-MRF.

2 | METHODS

2.1 | B1-MRF sequence

A gradient echo-based MRF sequence with RF and gradient spoiling (FLASH) and radial readout based on

a previously developed sequence²⁸ was applied. While FLASH achieves high spoiling efficiency at low FA steady-state imaging, transient states, high FA, and short TRs cause signal deviations from the approximation²⁹ that are addressed here by including T_2 sampling in the dictionary along with T_1 and B_1^+ . TE was kept fixed, and thus the T_2^* decay until readout results in a constant reduction of the signal in each time frame (TF). Similarly, chemical shift leads to a constant phase accumulation at readout for each TF. Together, these factors result in a complex scaling factor of the MRF signal curve that is matched independently of other parameters during MRF reconstruction.

The sequence employs 600 TFs, each corresponding to one TR interval, with a varying FA based on Jiang et al.'s pattern.³⁰ Diverging from previous methods,^{16,21,23,25,30}

adiabatic inversion was excluded because the maximum B_1^+ that would be required is above the amplifier limit. This minimizes T_1 sensitivity and reduces SAR. The acquisition train with identical FA pattern is repeated subsequently to acquire multiple spokes of each TF. The repetition of the entire FA pattern is referred to as a cycle (CYC). To avoid pauses in between the cycles, the FA pattern is played out continuously. In this work, 5–13 CYCs have been used. One additional dummy CYC is played out prior to the first CYC to ensure identical magnetization at the start of each subsequent CYC.

B1-MRF acquisition parameters are listed in Table 1. An 84° quadratic RF spoil increment was used for better transient state spoiling,³¹ and spoil gradients for an 8π -dephasing across the slice were applied. A golden angle k-space readout increment of 111.25° was used in between

TABLE 1 Acquisition parameters of phantom and in vivo studies with TR, TE, acquisition time (TA), FA, slice thickness, FOV, and pixel/voxel size, RF pulse, MRF cycles.

Phantom	B1-MRF	PEX	satTFL	AFI	BSS
TR/ms	4.4	6000	5000	20/100	553
TE/ms	2.2	2.7	2.42	1.85	14.0
TA	37 s	1 h 10 min 24 s	10s	6 min 12 s	1 min 11 s
Nominal FA $\alpha_{\max}^{\text{nom}}$ or $\alpha^{\text{nom}}/^\circ$	5, 7.5, 10, 15, 20, 30, 40, 50, 60, 70, 80		5, 8, 10, 15, 20, 30, 40, 50, 60, 80, 100, 120, 140, 160, 180	5, 8, 10, 15, 30, 40, 50, 60, 80, 100	5, 8, 10, 15, 20, 30, 40, 50, 60, 80 (250 μ s rect pulse)
Reference voltage (1Tx)/V	60		60	60	60
Slice thickness/mm	5	5	5		5
FOV/mm ² or mm ³	512 × 512	256 × 128	256 × 256	128 × 128 × 240	128 × 128
Pixel/voxel size/mm ² or mm ³	2 × 2	2 × 2	2 × 2	2 × 2 × 5	2 × 2
RF pulse type	Sinc (TBW = 4)	Rectangular	Rectangular	Rectangular	Fermi 8 kHz
RF pulse duration/ms	1	0.5	0.3	0.5	8
MRF cycles	13				
In vivo	B1-MRF		satTFL		RPE-AFI (3D)
TR/ms	4.4		5000		10/50
TE/ms	2.2		2.42		2.0
TA	16 s		10s		6 min 9 s
Nominal FA $\alpha_{\max}^{\text{nom}}$ or $\alpha^{\text{nom}}/^\circ$	60		180		80
Reference voltage (1Tx)/V	478		478		478
Slice thickness/mm	5		5		
FOV/mm ² or mm ³	512 × 512		384 × 264		320 × 320 × 256
Pixel/voxel size/mm ² or mm ³	2 × 2		2 × 2		4 × 4 × 4
RF pulse type	Sinc (TBW = 4)		Rectangular		Rectangular
RF pulse duration/ms	1.3		1.0		0.5
MRF cycles	5				

two CYCs of the same TF (Figure 1). The golden angle increment was also used from the last CYC of one TF to the first CYC of the next TF. The readout angle θ is then defined as $\theta = (i_{\text{CYC}} + i_{\text{TF}} \cdot N_{\text{CYC}}) \cdot 111.25^\circ$, where $i_{\text{CYC}}/i_{\text{TF}}$ denotes the index of the CYC/TF and N_{CYC} is the total number of cycles.

2.2 | Dictionary calculation

The dictionary was generated using 1D-Bloch simulations with 1601 isochromats, covering four times the nominal slice thickness to account for slice profile and spoiling effects. 67 200 entries with unique combinations of B_1^+ , T_1 , and T_2 were included: B_1^+ was included as a relative weighting factor applied to the nominal FA, ranging from 0.01 to 3.0 in 0.01 increments. T_1 ranged from 50 ms to 3446 ms, with T_1 increased successively by 8% relative to the previous value. T_2 values of [60, 80, 120, 150]ms were included.

Two CYCs were used to create the dictionary. The first CYC (dummy cycle) was necessary to obtain the initial magnetization of the consecutive repetition. The signal from the second CYC was then stored in the dictionary as a fingerprint (Figure 1).³² The dictionary entries were normalized to yield a sum of squared magnitude of 1.

2.3 | Image reconstruction

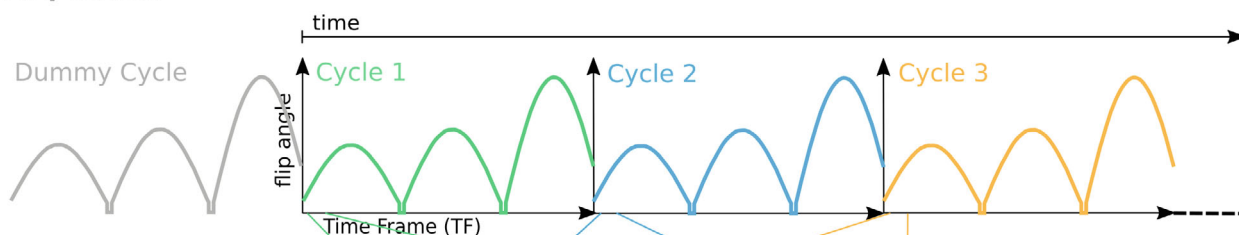
Acquired data of the same TF from different CYCs were binned together for image reconstruction (Figure 1). Thus, the number of spokes per TF is equal to the number of CYCs. A non-uniform fast Fourier transform was performed for each TF using *finufft*^{33,34} in *Python*.

MRF dictionary matching was performed by calculating the dot product in between the signal curve of each pixel and all curves of the dictionary. The image was masked to exclude areas only containing noise. For the in vivo scan, image reconstruction took 61 s and brute force MRF matching took 0.7 s on our reconstruction server (2x Intel Xeon E5-2687W v4, 24 cores, 1 TB RAM, up to 30 GB RAM used during reconstruction). Each pixel was then assigned the B_1^+ , T_1 , and T_2 values that were used to create the dictionary entry with the maximum dot product.¹⁶

2.4 | Imaging experiments

Phantom and in vivo MR scans were performed on a 7T scanner (Magnetom 7T, Siemens Healthineers, Erlangen, Germany). For the phantom experiments, a commercial 1Tx/32Rx head coil (Nova Medical, Wilmington, MA, USA) was used. Here, only the 1Rx birdcage of the coil was

(A) Acquisition



(B) k-space binning

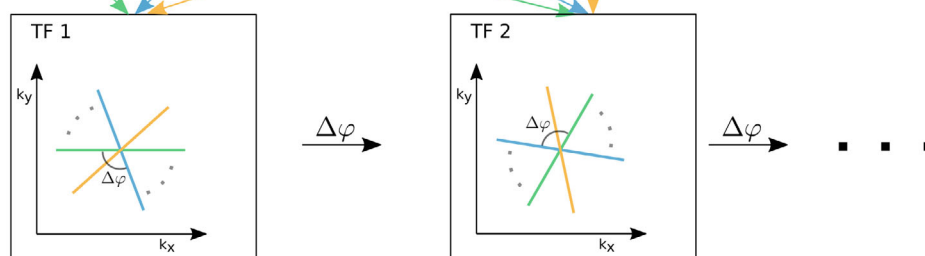


FIGURE 1 Overview of the acquisition of the proposed B1-MRF sequence: (A) The FA pattern is repeated several times (referred to as Cycle [CYC]) and a dummy CYC is played out prior to Cycle 1 to ensure the same initial magnetization at the beginning of each consecutive CYC. Each CYC contains 600 TR, referred to as TF. (B) Displays the k-space binning used for image reconstruction. For one TF, successive CYCs have a golden angle k-space increment of $\Delta\varphi = 111.25^\circ$. From the last CYC of one TF to the first CYC of the next TF, an increment of 111.25° is also applied. The readout angle θ is defined as $\theta = (i_{\text{CYC}} + i_{\text{TF}} \cdot N_{\text{CYC}}) \cdot 111.25^\circ$, where $i_{\text{CYC}}/i_{\text{TF}}$ denotes the index of the CYC/TF and N_{CYC} is the number of cycles.

used for reception, as distortions of the rectangular pulse shapes used by the reference methods had been observed during the first 100 μ s of the pulse when using the 32Rx array mode (Supporting Information Figure S1A). For B1-MRF, this effect is negligible because the RF amplitude is low during the first 100 μ s. However, for consistency, the 1Rx mode was also used for the B1-MRF phantom experiments and the number of cycles was increased compared to the in vivo scans (see Table 1). The B1-MRF maps of the phantom scans were multiplied by a factor of 0.975, as a constant RF amplitude increase of 2.5% was observed after the first CYC of the MRF FA pattern (yellow line in Supporting Information Figure S1B). Note, that the Cycle was not used for reconstruction (dummy CYC). Tubes 1, 4, 7, 9, 14, and 18 of the Eurospin TO5 phantom³⁵ were inserted into a phantom holder filled with water and a gadolinium-based contrast agent (GBCA). The tubes are made of agarose doped with GBCA. T_1 reference values were acquired at 7T using an inversion recovery spin-echo echo-planar imaging sequence with adiabatic inversion pulses and nine different TI times ([25, 50, 100, 200, 400, 800, 1600, 3200, 4800]ms). T_1 was fitted per pixel with a three-parameter model (T_1 , M_0 , M_z after inversion) and analyzed over a region of interest (ROI) centered on the tubes, yielding T_1 times of [204, 504, 642, 835, 1195, 1692]ms.

In vivo scans were performed in the body according to an approved Institutional Review Board protocol and healthy subjects were scanned after written informed consent. The scans were performed on three subjects (two males and one female, 27–34 years, 18.1–27.5 kg/m²) using a commercial 32-element body array (MRI.TOOLS, Berlin, Germany) in 1Tx/32Rx mode with the shim setting optimized by the coil manufacturer.

2.5 | Reference methods

To validate the accuracy of B1-MRF, phantom experiments were compared to a slow but precise 2D preparation-based method,³⁶ hereafter referred to as PEX. For dynamic range evaluation, the linearity of B1-MRF over different nominal FAs was compared with satTFL, AFI, and BSS using the same phantom. satTFL and AFI measure the actual FA, while BSS measures the B_1^+ field. To compare the results, we followed the approach of Pohmann and Scheffler¹³ and calculated the FA generated by a 250 μ s rectangular pulse with the measured peak B_1^+ of BSS. For in vivo reference, satTFL was acquired during breath hold and an AFI with radial-phase encoding (RPE-AFI)¹⁵ was obtained during free breathing.

PEX was acquired with non-selective 0.5 ms long rectangular preparation pulses. Eleven images with different

varying preparation amplitude (u_{RF}) from 0 V to 100 V in 10 V steps were acquired. Following the preparation pulse, a gradient spoiler was applied for 5 ms followed by a single line k-space readout for each image. Long TRs were used (6 s) to reach equilibrium magnetization before acquisition of the next k-space line. Further details on the PEX sequence and reconstruction are given in Supporting Information Note S1. Additional acquisition parameters for PEX and the other references are given in Table 1.

The B_1^+ maps in the Results section were normalized to the square root of 1 kW of input RF power (unit: μ T/ $\sqrt{\text{kW}}$), thus reflecting the B_1^+ efficiency. In contrast, for theoretical considerations of the fingerprint evolution of B1-MRF and for experiments at different input power levels where no spatial variation is displayed, the actual FA are displayed in units of degrees. For B1-MRF, the actual FA varies throughout the 600 actual FAs, therefore we denote the maximum actual FA of B1-MRF as a single scalar value per voxel. The term $\alpha_{\max}^{\text{nom}}$ refers to the maximum *nominal* FA specified in the sequence protocol, while α_{\max} refers to the measured maximum *actual* FA (cf. Figure 2A).

During in vivo acquisition, peak RF amplitudes were at or near the system maximum of 478 V (1Tx) for all acquisitions. A conservative power-controlled monitoring mode was employed for safety purposes, which limits the RF power per Tx channel.³⁷ The power limits correspond to worst-case 10 g averaged local SAR values according to IEC guideline limits. The in vivo scans reached 39%/1%/32% of the 10s limit and 7%/1%/80% of the 6 min limit for B1-MRF/satTFL/RPE-AFI.

3 | RESULTS

3.1 | Signal sensitivity to α_{\max} and T_1

Figure 2 evaluates the sensitivity of the MRF signal evolution to α_{\max} and T_1 . The actual FAs that are experienced by the magnetization (Figure 2A) during the acquisition are plotted together with the fingerprint evolution for a fixed $\alpha_{\max} = 20^\circ$ and different T_1 values (Figure 2B). The T_1 examined are 500 ms, 1300 ms and 2100 ms. Figure 2C shows the evolution of the normalized fingerprint for a fixed $T_1 = 1300$ ms and different α_{\max} in a low FA range. As can be seen qualitatively, changes in α_{\max} result in stronger changes in the normalized signal curve compared to changes in T_1 . Focusing on the normalized signal difference at TF 518, corresponding to α_{\max} , an 8.0% signal decrease is observed from $\alpha_{\max} = 5^\circ$ to $\alpha_{\max} = 10^\circ$ and a 33.2% decrease is observed from $\alpha_{\max} = 5^\circ$ to $\alpha_{\max} = 20^\circ$. For T_1 , these normalized signal changes are relatively smaller

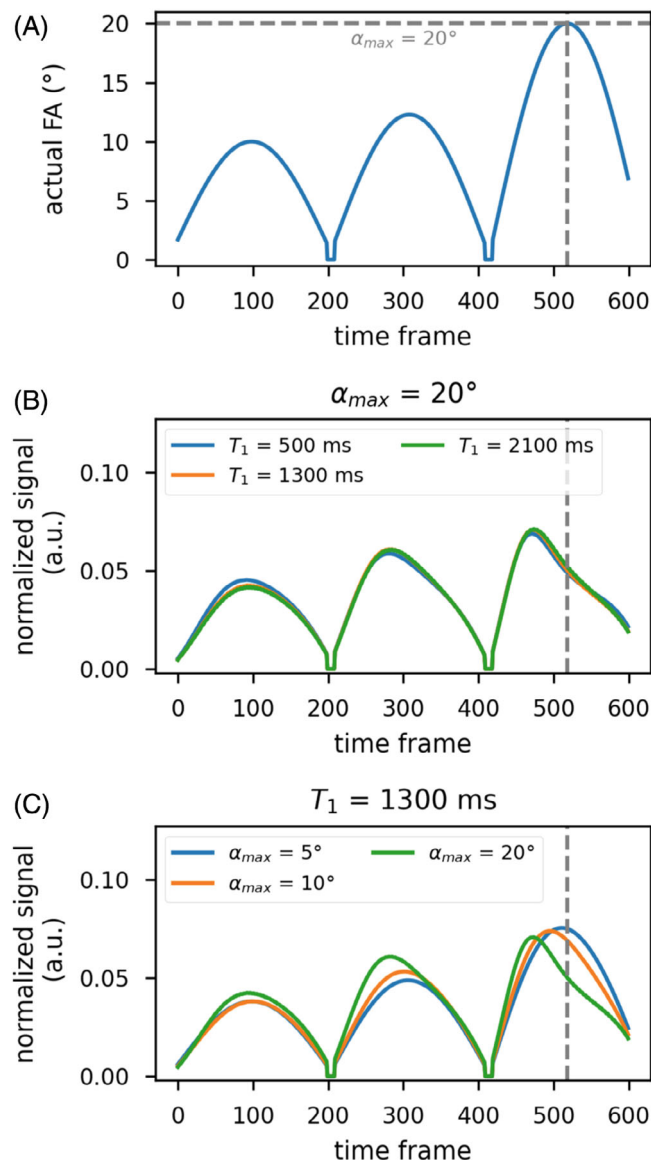


FIGURE 2 Sensitivity evaluation of B1-MRF. (A) The actual FAs experienced by the magnetization are position dependent. For this example, the actual FAs of a pixel are in the range of 0° – 20° . For simplicity, the actual FA for B1-MRF is expressed as the maximum FA experienced by the magnetization (α_{max}). (B) For a fixed α_{max} , the changes in signal magnitude for different T_1 times are small compared to (C), where the T_1 time is fixed and different α_{max} are considered.

with an increase of 2.4% from $T_1 = 500$ ms to $T_1 = 1300$ ms and an increase of 6.0% from $T_1 = 500$ ms to $T_1 = 2100$ ms. Supporting Information Figure S2 shows the Cramér-Rao bound for T_1 and α_{max} , which provides a more exhaustive evaluation over a larger parameter range. Supporting Information Figure S3 shows how a linear ΔB_0 gradient in the slice direction alters the signal curve. Mean deviations for $\alpha_{max} \leq 60^\circ$ were below 1.43% for a 50 Hz-range compared to 0 Hz.

3.2 | Phantom scans

Figure 3 shows the experimental validation of B1-MRF with the PEX method using the Eurospin TO5 tubes. For the PEX method, the fitting of the signal curve failed at the phantom edges where the FA is below $\sim 70^\circ$ for the maximum preparation voltage. In the phantom tubes, however, a quantitative comparison between both methods was feasible (see Figure 3A left). The results for both methods agree for $\alpha_{max}^{nom} = 30^\circ$ as shown by the line plots and a mean difference of $0.94 \pm 1.36 \mu T / \sqrt{kW}$ is observed over the area covered by PEX. For a quantitative analysis over a larger FA range B1-MRF was repeated with different nominal FAs (Table 1) and then compared with the corresponding values obtained by the PEX method (Figure 3B). PEX was acquired only once and provides the B_1^+ field per square root of input RF power, from which the actual FA at the different α_{max}^{nom} of B1-MRF was obtained as described in Supporting Information Note S1. FAs in the range of 0° – 70° are considered for the analysis. The coefficient of determination (r^2) in between the two methods for $T_1 = [204, 503, 642, 834, 1194, 1691]$ ms is $[0.998, 0.997, 0.999, 0.998, 0.995, 0.993]$, respectively. The slopes of a linear fit are $[0.96, 0.96, 0.96, 0.95, 0.96, 0.94]$, resulting in a linear drift from left to right. For FAs $< 10^\circ$, the mean absolute difference between the two methods evaluated per pixel in the ROIs is less than 4.92% when all tubes are evaluated separately. Only for the tube with $T_1 = 1691$ ms a larger difference of 8.33% is observed. The tube with $T_1 = 1691$ ms also has the largest mean absolute difference for FAs $> 50^\circ$ of 5.00%, while all other tubes are below 3.86%. In the range $10^\circ < FA < 50^\circ$, the mean absolute differences are below 2.29% for each individual tube.

Figure 4 shows the linearity of B1-MRF, satTFL, AFI and BSS (Figure 4A–D) over an FA range of 0° – 100° where each pixel in the center of the tubes is evaluated (29 pixels per tube) for all tubes (i.e., all T_1 values). Here, as a reference, one scan of the same method was used in a range where the respective method is accurate. To obtain the scatter plot, the scan was repeated with different nominal FA (Table 1) and then the individual pixels (y-axis) are plotted against the reference scaled to the nominal FA (x-axis). The reference scan in Figure 4A was B1-MRF with $\alpha_{max}^{nom} = 30^\circ$, where the obtained FA values in a range from $\alpha_{max} = 24^\circ$ – 60° are in the range where B1-MRF is accurate (cf. Figure 3). B1-MRF scans with a different α_{max}^{nom} value (e.g., 60°) were then obtained and compared to the B1-MRF reference scan, for which the reference scan was scaled by the ratio of the different α_{max}^{nom} values (e.g., factor 2). For satTFL, AFI, and BSS (Figure 4B–D), a reference scan with a nominal preparation FA of $\alpha^{nom} = 60^\circ/80^\circ/60^\circ$ (satTFL/AFI/BSS) of the

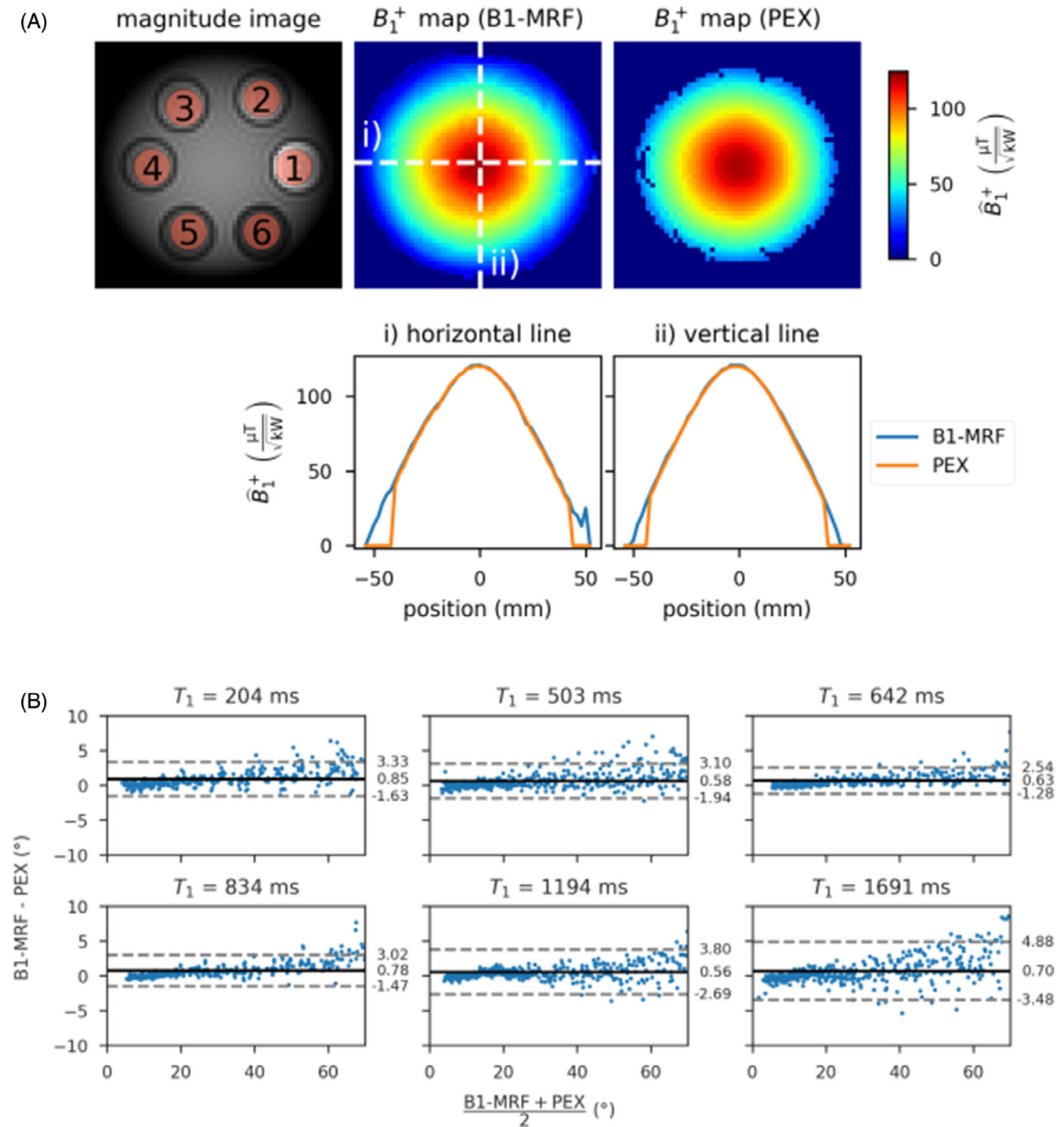


FIGURE 3 Validation of B1-MRF with a preparation-based reference (PEX) in tubes of the Eurospin TO5 phantom³⁵ with different T_1 using a commercial head coil at 7T. (A) FA maps of the phantom for B1-MRF and PEX with a vertical and horizontal line plot. Mean difference of $0.65 \pm 0.94^\circ$ in the area covered by PEX. (B) Bland-Altman plots of the two methods, where B1-MRF was acquired with 11 different nominal FAs and PEX was acquired only once and scaled accordingly. For $T_1 = 204$ ms–1194 ms at $\alpha_{\max} < 10^\circ$, the pixel-wise difference is $< 2.99 \pm 8.06\%$ when each tube is considered separately ($T_1 = 1691$ ms: Difference $7.95 \pm 19.91\%$). In the range $10^\circ < \alpha_{\max} < 50^\circ$, the deviations are below $2.29 \pm 4.27\%$ for each individual tube.

respective method was selected which yielded a measured FA range of $\alpha = 42^\circ$ – $117^\circ/46^\circ$ – $145^\circ/38^\circ$ – 111° . The measured FA range of the reference scan is in the range

where the method showed highest linearity. The reference scans were then multiplied by the ratio of the nominal FAs, as for B1-MRF. For satTFL, the readout FA was of

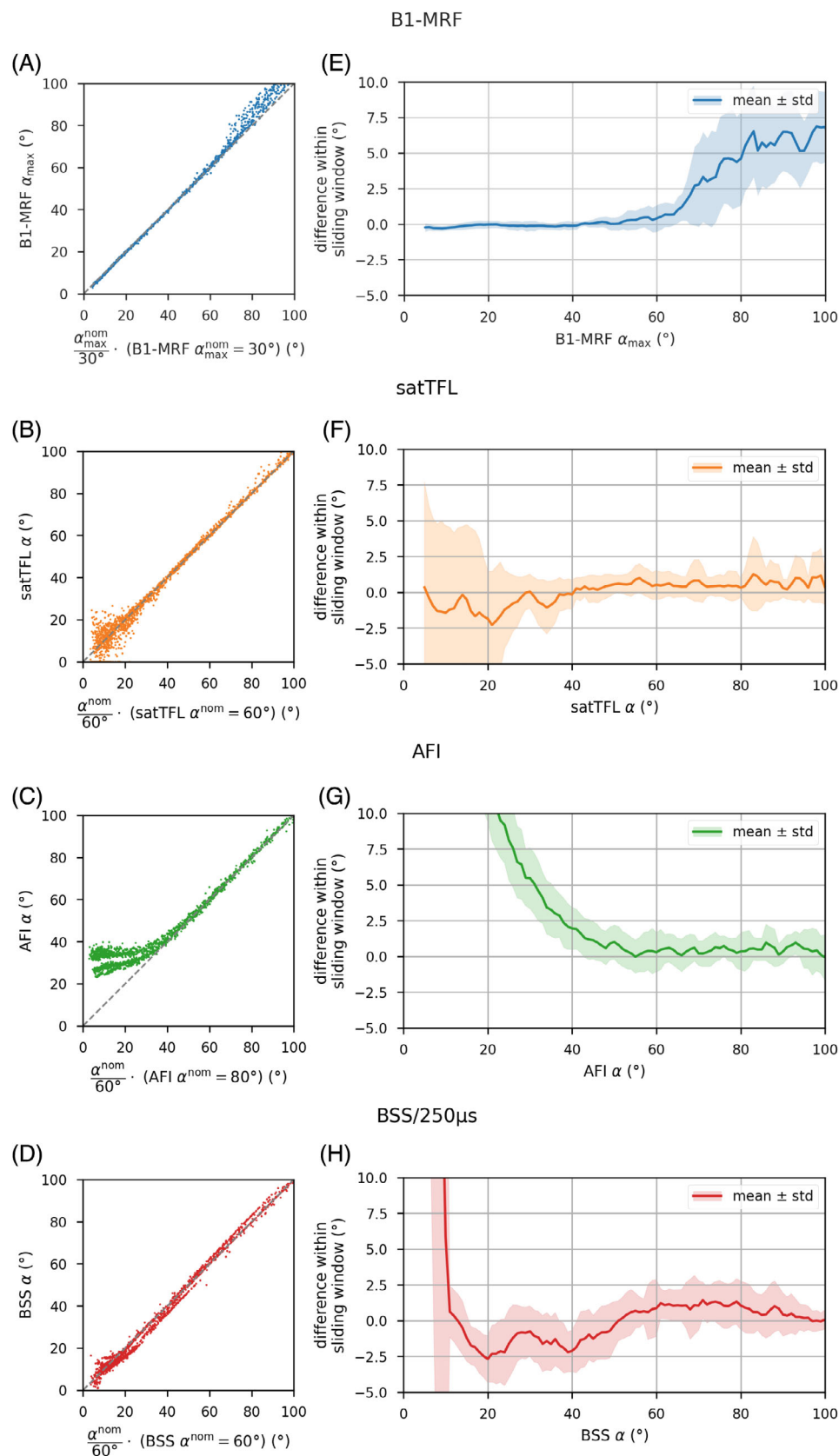


FIGURE 4 Linearity evaluation for B1-MRF, satTFL, AFI, and BSS in an FA range from 0° to 100° . (A–D) Measured data at different nominal FAs compared to a scan with a nominal FA that lies in the linear range of the method. The comparison scan was scaled with the factor in between nominal FA of the respective acquisition and the nominal FA of the comparison scan to create the plot. The reference scans were: B1-MRF with $\alpha_{max}^{nom} = 30^\circ$ (measured α_{max} range 24° – 60°), satTFL with $\alpha^{nom} = 60^\circ$ (measured α range 42° – 117°), AFI with $\alpha^{nom} = 80^\circ$ (measured α range 46° – 145°), BSS (FA calculated for a $250 \mu s$ rectangular pulse) with $\alpha^{nom} = 60^\circ$ (measured α range 38° – 111°). The dashed gray line is the identity line. B1-MRF (A) has good linearity at low FAs, while satTFL, AFI, and BSS (B–D) have good linearity at high FAs. (E–H) The mean \pm SD from the identity line in (A–D), where a rectangular sliding window of 3° width was applied. For B1-MRF (E) the deviation is $<4.7 \pm 4.7$ in the range of 6° – 74° , while for satTFL, AFI, BSS (F–H), the deviations are up to $16.4 \pm 108.2\%$, $409.1 \pm 71.2\%$, $1242.4 \pm 924.6\%$ in the same range, respectively. For $50^\circ < FA < 100^\circ$, the deviations of satTFL, AFI, BSS (F–H) are $<1.8 \pm 3.1\%$, $<2.0 \pm 2.7\%$, $<2.0 \pm 3.4\%$, respectively, while for $74^\circ < FA < 100^\circ$ the deviation in B1-MRF (C) is up to $7.9 \pm 4.5\%$.

10% of the preparation FA and for BSS the readout FA was $1.35^\circ/\mu T$ (nominal peak B_1^+ of the Fermi pulse). For AFI, there is no additional readout pulse. Figure 4E–H

show the deviation from the identity line of Figure 4A–D, where a rectangular sliding window of 3° width was used for evaluation of the difference, resulting in mean \pm SD

values. The sign of the deviation was retained for the calculation of these values, enabling the visualization of the direction of the deviation. Focusing on the deviation, the B1-MRF approach shows linear behavior in a range of 6° – 74° , where the $|\text{mean}| \pm \text{SD}$ is $<4.7 \pm 4.7\%$. For the same range, the $|\text{mean}| \pm \text{SD}$ for the reference methods is up to $16.4 \pm 108.2\%/409.1 \pm 71.2\%/1242.4 \pm 924.6\%$ (satTFL/AFI/BSS). For FAs above 50° , the references appears linear with $|\text{mean}| \pm \text{SD}$ deviations $<1.8 \pm 3.1\%/2.0 \pm 2.7\%/2.0 \pm 3.4\%$, whereas for FAs above 74° , $|\text{mean}| \pm \text{SD}$ up to $7.9 \pm 4.5\%$ are visible in B1-MRF. The upper boundary for which the deviation from the identity line evaluated by $|\text{mean} \pm \text{SD}|$ is smaller for B1-MRF as for the references amounts to 61° , 65° , 67° compared to satTFL, AFI, BSS, respectively. A dynamic range is calculated with the condition $|\text{mean} \pm \text{SD}| \leq \epsilon$, where the relative mean and SD are used (Supporting Information Figure S4). For $\epsilon = 10\%$, a dynamic range of $12.3(6^{\circ}$ – $74^{\circ})$ is observed for B1-MRF and $5.0(27^{\circ}$ – $136^{\circ})/4.6(39^{\circ}$ – $180^{\circ})/3.3(36^{\circ}$ – $120^{\circ})$ for satTFL/AFI/BSS, respectively.

Figure 5 examines the effect of the number of CYCs on the \hat{B}_1^+ map and the resulting artifacts are investigated for different resolutions. Maps are considered artifact free if no discontinuities are visible: (i) for individual pixels; and (ii) due to aliasing artifacts propagating from the undersampled MRF images to the \hat{B}_1^+ maps. Note that for the $(1 \times 1) \text{ mm}^2$ resolution, TE/TR had to be increased to 3.5/7.0 ms due to peripheral nerve stimulation limits, as the protocol was set up to be applicable to in vivo

acquisitions. For a $(4 \times 4) \text{ mm}^2$ resolution, no artifacts are observed at 5 CYC. For $(2 \times 2) \text{ mm}^2$ resolution, single pixel discontinuities are observed for 5 CYC, mostly appearing at the edge of the phantom. The artifacts disappear for ≥ 5 CYC. At $(1 \times 1) \text{ mm}^2$ resolution, maps without artifacts are observed only for 13 CYC. For these measurements, the 1Rx birdcage receive mode of the coil was used with lower SNR at the edges of the phantom. A comparison between the 1Rx and the 32Rx mode, which provides higher SNR and which would be applied in-vivo, is provided in Supporting Information Figure S5 for the $(2 \times 2) \text{ mm}^2$ resolution. Note, that the MRF sequence is barely affected by the distortions during the first 100 μs of the pulse shown in Supporting Information Figure S5. No artifacts are observed in the B1-MRF maps even at 5 CYC for a resolution of $(2 \times 2) \text{ mm}^2$.

3.3 | In vivo abdominal scans

Figure 6 shows the comparison with satTFL and RPE-AFI in the abdomen for three volunteers with different body mass index (BMI) values ($[18.1, 25.5, 27.5] \text{ kg/m}^2$) in $\mu\text{T}/\sqrt{\text{kW}}$ (defined as \hat{B}_1^+). Qualitatively, the highest agreement between the different approaches is observed for volunteer 1 (BMI = 18.1 kg/m^2). For volunteers 2 and 3 agreement can be observed in parts of the liver close to the coil elements where relatively higher \hat{B}_1^+ is obtained, while discontinuities appear in low \hat{B}_1^+ regions. These discontinuities, however, are less pronounced in the B1-MRF

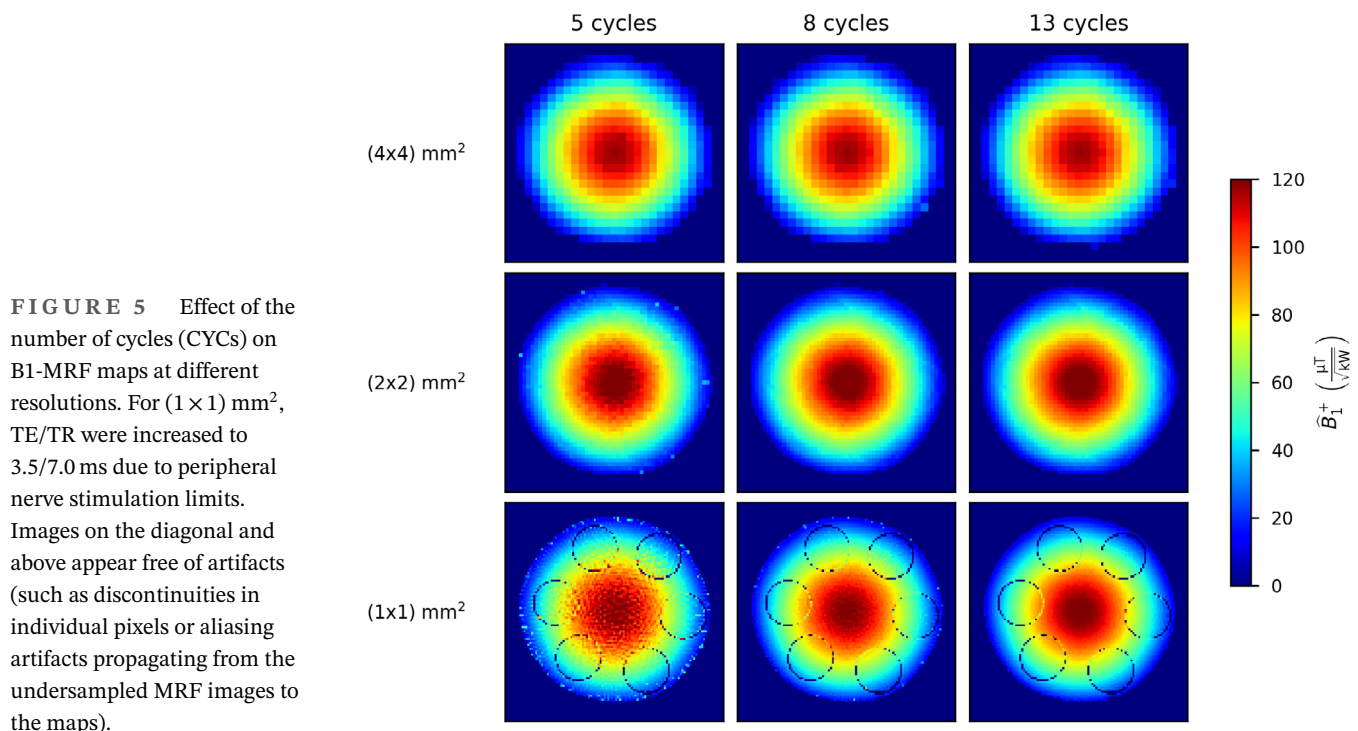


FIGURE 5 Effect of the number of cycles (CYCs) on B1-MRF maps at different resolutions. For $(1 \times 1) \text{ mm}^2$, TE/TR were increased to 3.5/7.0 ms due to peripheral nerve stimulation limits. Images on the diagonal and above appear free of artifacts (such as discontinuities in individual pixels or aliasing artifacts propagating from the undersampled MRF images to the maps).

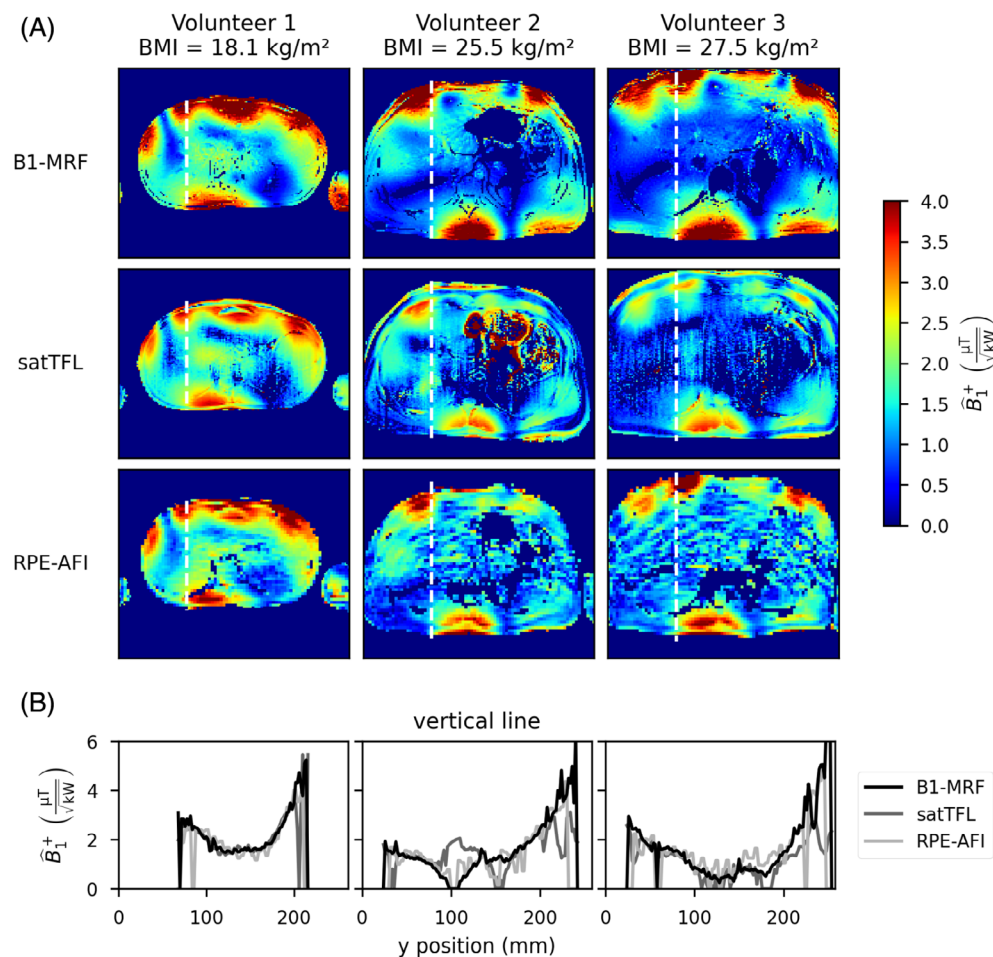


FIGURE 6 In vivo abdominal scans at 7T for three volunteers for B1-MRF, satTFL, and RPE-AFI. (A) Maps are shown in $\mu\text{T}/\sqrt{\text{kW}}$. For volunteer 1 (18.1 kg/m^2), a good agreement between the different approaches can be observed, as shown by the vertical line (B). For volunteer 2 and 3 ($\geq 25.5 \text{ kg/m}^2$), inconsistencies are visible in low FA regions of satTFL and RPE-AFI that are not visible in B1-MRF. In the line plot (B), this is evident in larger discrete jumps for satTFL and RPE-AFI compared to B1-MRF.

maps. The plot of the vertical line (Figure 6B) highlights the differences. For volunteer 2 and 3, larger discrete steps from one pixel to the next can be observed for satTFL and RPE-AFI compared to B1-MRF over the entire line. A large offset in between the methods occurs on the right side of the line plots where subcutaneous fat is located. Here, B1-MRF yields higher \hat{B}_1^+ values compared to the reference methods. This is examined in more detail in Figure 7 for the back fat region. Supporting Information Figure S6A shows the T_1 map obtained by the B1-MRF matching step for volunteer 1. The map reveals elevated T_1 values ($>2000 \text{ ms}$) in the center of the liver, which is inconsistent with findings of a 7T spectroscopy study reporting $T_1 = 1362 \text{ ms}$ for the water peak of liver tissue.³⁸ The low sensitivity of the \hat{B}_1^+ maps to mismatched T_1 is shown in Supporting Information Figure S6. Here, an average bias of -1.50% in the \hat{B}_1^+ maps is observed from the T_1 matched by B1-MRF to a T_1 of 1368 ms (Subfigure A). In addition, a simulation study (Subfigure B) was performed to estimate the effect of a mismatched T_1 on \hat{B}_1^+ as a function of a T_1 error from -50% to 50% . For $\hat{B}_1^+ \leq 1.5 \mu\text{T}/\sqrt{\text{kW}}$, where the T_1 estimation capability is reduced compared to higher \hat{B}_1^+ ,

a maximum \hat{B}_1^+ error of 4.1% was found for $1.5 \mu\text{T}/\sqrt{\text{kW}}$ at a T_1 error of 50% .

Figure 7 displays a zoomed-in view of the high \hat{B}_1^+ region on the back of the volunteers. Strong deviations of measured \hat{B}_1^+ are observed in the different methods in the region close to the skin where subcutaneous fat is expected. The highest \hat{B}_1^+ values are observed for B1-MRF, followed by RPE-AFI, and the lowest \hat{B}_1^+ values are observed for satTFL. Moving from posterior to anterior, satTFL and RPE-AFI first reflect an area of high \hat{B}_1^+ values, followed by local minima before reaching higher \hat{B}_1^+ again. In contrast, no local minima appear close to the skin for B1-MRF. Focusing on the maximum measured \hat{B}_1^+ excluding the outermost skin layer, for volunteer 1 reveals values of $4.94 \mu\text{T}/\sqrt{\text{kW}}$, $3.78 \mu\text{T}/\sqrt{\text{kW}}$ and $4.49 \mu\text{T}/\sqrt{\text{kW}}$ for B1-MRF, satTFL, and RPE-AFI, respectively (volunteer 2: $6.62 \mu\text{T}/\sqrt{\text{kW}}$, $3.57 \mu\text{T}/\sqrt{\text{kW}}$, $4.90 \mu\text{T}/\sqrt{\text{kW}}$; volunteer 3: $6.30 \mu\text{T}/\sqrt{\text{kW}}$, $3.59 \mu\text{T}/\sqrt{\text{kW}}$, $4.95 \mu\text{T}/\sqrt{\text{kW}}$). On average, the maximum observed \hat{B}_1^+ is 37% lower for satTFL and 18% lower for RPE-AFI compared to B1-MRF.

Figure 8 shows a quantitative comparison between the methods in a Bland–Altman plot. For each volunteer, an

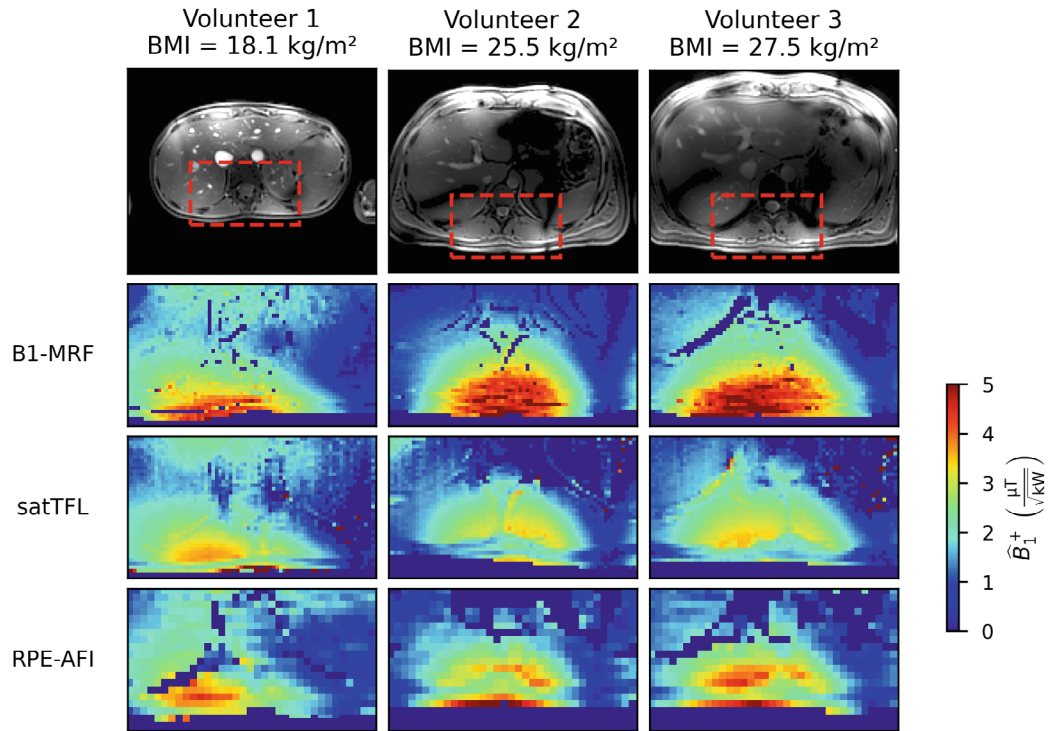


FIGURE 7 Zoom on the high \hat{B}_1^+ posterior region of Figure 6, where subcutaneous fat is located. The zoom region is marked by the red dotted line on the magnitude images in the first row. Strong differences are observed between the different methods, where the highest \hat{B}_1^+ values are observed for B1-MRF, followed by satTFL and the lowest values are observed for RPE-AFI. B1-MRF uses 1.3 ms sinc pulses with a time-bandwidth product of 4, while satTFL and RPE-AFI use rectangular pulses of 1 ms and 0.5 ms, respectively. The rectangular pulses result in less fat proton excitation due to the 1 kHz off-resonance of the dominant fat peak. In addition, satTFL and RPE-AFI use Cartesian encoding, resulting in shifts along the frequency encoding direction for fat, whereas incoherent shifts of the radial encoding of B1-MRF are favorable in the presence of fat.

ROI (red area in the magnitude images) is defined within the liver and only pixels with non-zero \hat{B}_1^+ values in both methods are considered. The absolute mean difference is $\leq 0.18 \mu\text{T}/\sqrt{\text{kW}}$ for all comparisons. The lowest SD between B1-MRF and the references is observed for volunteer 1 (satTFL: $0.22 \mu\text{T}/\sqrt{\text{kW}}$, RPE-AFI: $0.27 \mu\text{T}/\sqrt{\text{kW}}$), while for volunteers 2 and 3, it is in the range of $0.37 \mu\text{T}/\sqrt{\text{kW}} - 0.47 \mu\text{T}/\sqrt{\text{kW}}$ for satTFL and RPE-AFI. Focusing on the structure of the Bland–Altman plots, the spread around the mean line is reduced for $\hat{B}_1^+ > 2 \mu\text{T}/\sqrt{\text{kW}}$, except for satTFL for volunteer 3, which shows a positive deviation from the mean line. To compare the agreement between high $\hat{B}_1^+ > 2 \mu\text{T}/\sqrt{\text{kW}}$ and low $\hat{B}_1^+ < 2 \mu\text{T}/\sqrt{\text{kW}}$, an error ϵ with the condition $|\text{mean} \pm \text{SD}| \leq \epsilon$ can be obtained for each FA range where the relative mean and SD are calculated from the pixelwise difference to B1-MRF. The best agreement is obtained for volunteer 1, where limits of $\epsilon_{\text{satTFL}} = 8.5\%$; $\epsilon_{\text{RPE-AFI}} = 28.3\%$ for high \hat{B}_1^+ and $\epsilon_{\text{satTFL}} = 25.7\%$; $\epsilon_{\text{RPE-AFI}} = 48.5\%$ for low \hat{B}_1^+ is observed. The worst agreement of satTFL and RPE-AFI with B1-MRF was observed for low \hat{B}_1^+ regions in volunteer 2 and 3 with $50.7\% < \epsilon < 113.4\%$, whereas for high

\hat{B}_1^+ regions $14.7\% < \epsilon < 34.3\%$ for those volunteers. For all volunteers, an increase of the limit ϵ by a factor of 1.5–4.6 is observed going from high \hat{B}_1^+ values to low \hat{B}_1^+ values. Supporting Information Figure S7 provides statistical metrics of \hat{B}_1^+ , including mean, SD, and interquartile range. A statistically significant difference (Mann–Whitney U test, $p < 0.05$) was found between the \hat{B}_1^+ distributions of B1-MRF and satTFL/RPE-AFI in all comparisons, with the exception of the comparison between B1-MRF and satTFL for volunteer 1 ($p = 0.44$).

In Figure 9, the smoothness of the \hat{B}_1^+ maps is evaluated by the histogram of the gradients within two ROIs, where one is in a higher \hat{B}_1^+ area and one in a lower \hat{B}_1^+ area within the liver. The gradient is defined as the total differential and therefore a sum of the partial gradients $d\hat{B}_1^+ = \partial\hat{B}_1^+/\partial x \cdot \Delta x + \partial\hat{B}_1^+/\partial y \cdot \Delta y$ and is shown in Supporting Information Figure S8. A normal distribution with an additional scaling factor (so that the integral over the histogram does not have to equal 1) was fitted to the data. In the ROI of high \hat{B}_1^+ values, an SD $\sigma \leq 0.105 \mu\text{T}/\sqrt{\text{kW}}$ is observed for B1-MRF across all volunteers, $\sigma \leq 0.084 \mu\text{T}/\sqrt{\text{kW}}$ for satTFL and $\sigma \leq 0.201 \mu\text{T}/\sqrt{\text{kW}}$ for

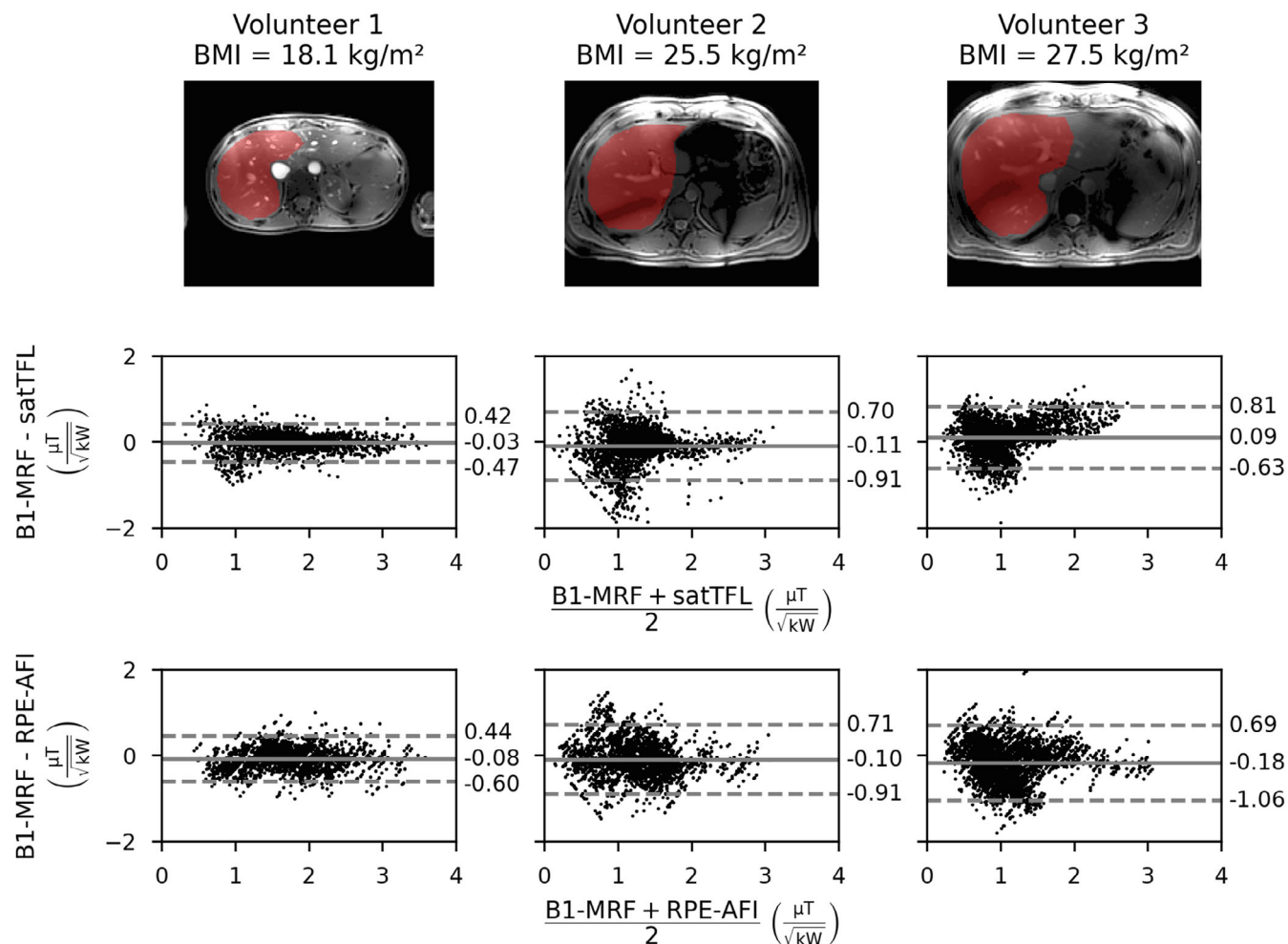


FIGURE 8 Quantitative comparison of B_1 -MRF with satTFL and RPE-AFI in a Bland–Altman plot for the liver of all volunteers. The magnitude images in the top row show the ROIs in red. The absolute mean difference is $\leq 0.18 \mu\text{T}/\sqrt{\text{kW}}$ for all comparisons. The lowest SDs are observed for volunteer 1 (satTFL: $0.22 \mu\text{T}/\sqrt{\text{kW}}$, RPE-AFI: $0.27 \mu\text{T}/\sqrt{\text{kW}}$), while for volunteers 2 and 3, they are in a range of $0.37 \mu\text{T}/\sqrt{\text{kW}} - 0.47 \mu\text{T}/\sqrt{\text{kW}}$ for both comparisons. In general, the SDs are lower for $\hat{B}_1^+ > 2 \mu\text{T}/\sqrt{\text{kW}}$ compared to $\hat{B}_1^+ < 2 \mu\text{T}/\sqrt{\text{kW}}$.

RPE-AFI. In the ROI of low \hat{B}_1^+ values, mostly larger SDs are observed compared to the high \hat{B}_1^+ ROI, with a factor of 1.6–3.3 for satTFL, 1.0–1.8 for RPE-AFI, and 1.3 for B1-MRF volunteer 1. For B1-MRF, volunteers 2 and 3 have lower SDs in the low \hat{B}_1^+ ROI compared to the high \hat{B}_1^+ ROI by a factor of 0.7 and 0.8, respectively.

4 | DISCUSSION

In this work, an MRF-based B_1^+ mapping sequence (B1-MRF) was developed and tested at 7T. The MRF signal curves show high sensitivity to changes in B_1^+ at FAs $< 20^\circ$, where previous approaches have low sensitivity.¹³ Phantom experiments validated B1-MRF's accuracy, showing a strong correlation with a very slow, yet precise reference method (PEX),³⁶ across an FA range of 0° – 70° , evidenced by a mean coefficient of determination $r^2 = 0.997$. The practical applicability of B1-MRF was further demonstrated

through in vivo abdominal scans conducted in three volunteers during breath-hold. The resulting B_1^+ -maps were compared with satTFL and RPE-AFI. For the volunteer with the lowest BMI (18.1 kg/m^2), B1-MRF aligned closely with satTFL and RPE-AFI. However, for the two volunteers with higher BMIs ($\geq 25.5 \text{ kg/m}^2$), the satTFL and RPE-AFI based B_1^+ -maps showed inconsistencies in low B_1^+ regions, while the B1-MRF results remained consistent across these areas.

A fundamental challenge in UHF body imaging is to accurately quantify FAs due to the typically lower B_1^+ efficiency of multichannel transmit arrays for the human body compared to transmit arrays for the head, and large FA measurements are often constrained by limited RF power and SAR restrictions. Therefore, the B1-MRF method, with its high accuracy and precision at low FAs, is promising for several UHF body applications. One such application is safety validation through electromagnetic field simulation. Since SAR, and thus tissue heating, is

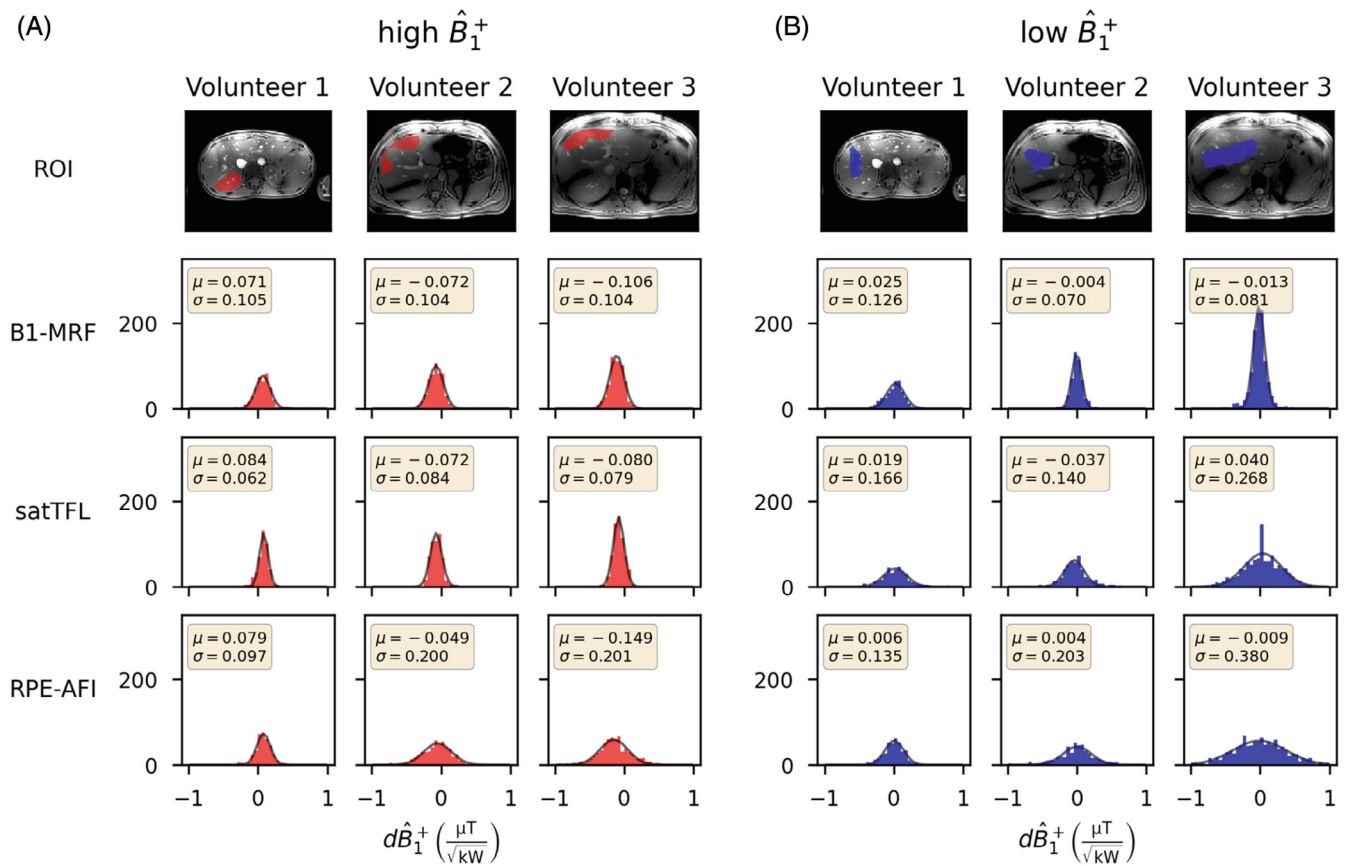


FIGURE 9 Histogram of the total differential over a high (A) and a low (B) \hat{B}_1^+ ROI in the liver. The total differential is defined as the sum of the partial gradients $d\hat{B}_1^+ = \partial\hat{B}_1^+/\partial x \cdot \Delta x + \partial\hat{B}_1^+/\partial y \cdot \Delta y$ and is shown in Supporting Information Figure S8. A normal distribution (black line) with an additional scaling factor (so that the integral over the histogram does not have to equal 1) was fitted to the data (red (A)/blue (B) bars). The x-axis shows the spatial change in \hat{B}_1^+ and the y-axis shows how often the values occurred, with the data discretized into 40 bins from -1 to 1 . In the high \hat{B}_1^+ ROI (A), an SD $\sigma \leq 0.105 \mu\text{T}/\sqrt{\text{kW}}$ is observed for B1-MRF across all volunteers, $\sigma \leq 0.084 \mu\text{T}/\sqrt{\text{kW}}$ for satTFL and $\sigma \leq 0.201 \mu\text{T}/\sqrt{\text{kW}}$ for RPE-AFI. In the low \hat{B}_1^+ ROI, mostly larger SDs are observed compared to the high \hat{B}_1^+ ROI, except for B1-MRF. Here, volunteers 2 and 3 have lower SDs in the low \hat{B}_1^+ ROI compared to the high \hat{B}_1^+ ROI by a factor of 0.7 and 0.8, respectively.

dependent on electromagnetic fields, accurate assessment is critical. While E -fields themselves cannot be measured directly in vivo, B_1^+ -fields can be quantified by B_1^+ mapping. These measurements can then be compared with simulation results to ensure safety,³ where high accuracy of B_1^+ -maps even in low FA regions is essential.³⁹ Another application is electrical property tomography, where electrical permittivity is encoded in the B_1^+ amplitude. The precision of B_1^+ -maps is important here, as a 1% error in the B_1^+ -map can lead to a 20% bias in permittivity estimates, impacting clinical viability.⁴⁰

The aim of this work was to investigate the feasibility and the accuracy of MRF-based B_1^+ mapping, which was demonstrated using a combination of all Tx channels, rather than channel-wise mapping. However, although further investigations are needed, preliminary results using a hybrid approach suggest that this method is principally suitable for channel-wise B_1^+ mapping.⁴¹

High accuracy and precision at low FAs of B1-MRF was demonstrated in the phantom experiments. In particular, a more than two-fold increase in dynamic range was found compared to satTFL, AFI, and BSS, which may be beneficial for applications with large B_1^+ variation beyond body imaging at UHF, such as head-and-neck B_1^+ mapping,⁴² which traditionally rely on multiple B_1^+ scans at varying reference amplitudes to achieve a greater dynamic range. The sensitivity analysis of the MRF signal evolution (Figure 2) and the Cramér-Rao bound (CRB) analysis (Supplementary Information Figure S2) show a high sensitivity to the FA across a large range, whereas the sensitivity to T_1 is comparably low, since preparation pulses and additional delays in between subsequent cycles that are typically applied for T_1 quantification are omitted.²⁵ Complete T_1 insensitivity cannot be achieved in MRF due to the intertwined nature of the parameters. The CRB analysis shows an increasing T_1 sensitivity with higher B_1^+ , implying that at low B_1^+ , the influence of T_1 is

minimal and errors due to mismatched T_1 are lower. This has been confirmed experimentally (Supporting Information Figure S6). In low B_1^+ regions of the liver, B1-MRF T_1 values differ significantly ($T_1 > 2000$ ms) from literature T_1 values of the liver,³⁸ while regions near the coil where B_1^+ is increased show results closer to such T_1 values. This is consistent with the CRB analysis (Supporting Information Figure S2A), indicating a low T_1 encoding capability at low FAs and suggesting a rather low sensitivity of B_1^+ values to T_1 . This rather low influence of T_1 on B_1^+ is experimentally confirmed in Supporting Information Figure S6 where a mean deviation of 1.5% was found for B1-MRF B_1^+ maps in liver tissue due to T_1 mismatch.

In vivo abdominal scans using B1-MRF show good agreement with satTFL and RPE-AFI in a low BMI subject. However, for individuals with higher BMI, reference methods display inconsistencies in low FA areas, in contrast to the typically smooth variations of the B_1 fields. This smoothness is quantified by lower SDs in B1-MRF's partial derivatives, despite its nominal FA values being lower (3 times and 1.33 times for satTFL and AFI, respectively). Substantial B_1^+ discrepancies are observed near the subcutaneous fat layer due to the 1 kHz off-resonance of the dominant fat peak (Figure 8). To evaluate the effect of ΔB_0 off-resonance on different sequences, it is necessary to consider (i) the effect of ΔB_0 on spin excitation and (ii) the ΔB_0 -induced phase accumulation at readout. Regarding (i) the FA results obtained with satTFL and AFI are ΔB_0 dependent as these methods apply non-selective preparation pulses for B_1^+ encoding. Bloch simulations (Supporting Information Figure S9) show that 1 ms and 0.5 ms rectangular pulses reduce the transverse magnetization at 1 kHz off-resonance by 96% and 21%, respectively, compared to on-resonant spins. B1-MRF, however, uses slice-selective B_1^+ encoding, causing a 1.62 mm slice shift of the 5 mm slice for 1 kHz off-resonant spins with the 1.3 ms sinc pulse (tbw 4). Regarding (ii) for global ΔB_0 offsets in B1-MRF, the phase accumulates uniformly along the slice while the signal magnitude remains unchanged. When considering linear ΔB_0 ramps along the slice for B1-MRF, the signal magnitude can be affected due to out-of-phase isochromats at readout. However, for small linear ΔB_0 ramps (<15 Hz within 5 mm^{43}), this effect is negligible for B1-MRF (Supporting Information Figure S3). The AFI and satTFL B_1^+ maps are generated by dividing two signals/images with the same TE and are therefore unaffected by phase accumulation variations. These ΔB_0 considerations also apply to the ΔB_0 off-resonances of the water peak, which are expected to occur within ± 400 Hz in the body at $7T^{43}$ (Supporting Information Figure S9).

In the development of the B1-MRF technique, accurate characterization of the RF transmission chain proved to be critical for accurate B_1^+ mapping. Pickup-loop measurements revealed distortions of the rectangular pulse shapes used in PEX during the first 100 μ s in the 32Rx mode, which was absent in the 1Rx mode (Supporting Information Figure S1A). The use of the 1Rx mode reduced the offset between B1-MRF and PEX by 4.2%. The pick-up coil experiments also revealed a 2.5% drift in the RF amplifier during B1-MRF, which was subsequently corrected, as described in the Methods section. Correction for these systematic errors resulted in a high level of agreement between B1-MRF and PEX.

Limitations of B1-MRF were observed at high FAs. For larger T_1 values ($T_1=1691$ ms), a decrease in accuracy was observed for $FAs > 40^\circ$ for the phantom

the power per channel is limited. Additionally, using trajectories that cover a larger k-space area in one TF, like spiral trajectories, could improve B1-MRF efficiency, although this necessitates addressing gradient nonlinearities in sequence design and/or image reconstruction.⁴⁸

5 | CONCLUSIONS

B1-MRF provides highly accurate and precise FA measurements, particularly in the 6°–74° range (maximum actual FA during MRF pattern) with a mean deviation of less than 5% from the reference measurement, making it well-suited for body imaging at 7T and beyond. Its increased sensitivity at low FAs, where previous methods have struggled, creates new opportunities in various applications, including safety validations, electrical properties tomography, and libraries for parallel transmission applications. The capabilities of B1-MRF address current challenges in UHF MRI and have the potential to push the boundaries of UHF body imaging.

ACKNOWLEDGMENTS

We thank Martijn Cloos, University of Queensland, Australia, for valuable discussions. We gratefully acknowledge funding from the German Research Foundation SCHM 2677/4-1 and GRK2260-BIOQIC. Open Access funding enabled and organized by Projekt DEAL.

ORCID

Max Lutz  <https://orcid.org/0009-0001-1956-3757>

Christoph Stefan Aigner  <https://orcid.org/0000-0003-3618-9610>

Sebastian Flassbeck  <https://orcid.org/0000-0003-0865-9021>

Felix Krueger  <https://orcid.org/0000-0001-9453-8992>

Christoph Kolbitsch  <https://orcid.org/0000-0002-4355-8368>

Berk Silemek  <https://orcid.org/0000-0001-8227-3632>

Frank Seifert  <https://orcid.org/0000-0002-7065-2528>

Sebastian Schmitter  <https://orcid.org/0000-0003-4410-6790>

REFERENCES

- Ljungberg E, Wood T, Solana AB, et al. Silent T1 mapping using the variable flip angle method with B1 correction. *Magn Reson Med*. 2020;84:813–824.
- Siversson C, Chan J, Tiderius CJ, et al. Effects of B1 inhomogeneity correction for three-dimensional variable flip angle T1 measurements in hip dGEMRIC at 3 T and 1.5 T. *Magn Reson Med*. 2012;67:1776–1781.
- Fiedler TM, Ladd ME, Bitz AK. SAR simulations & safety. *NeuroImage*. 2018;168:33–58.
- Katscher U, Börner P, Leussler C, van den Brink JS. Transmit SENSE. *Magn Reson Med*. 2003;49:144–150.
- Zhu Y. Parallel excitation with an array of transmit coils. *Magn Reson Med*. 2004;51:775–784.
- Vaughan Jt, Garwood M, Collins CM, et al. 7T vs. 4T: RF power, homogeneity, and signal-to-noise comparison in head images. *Magn Reson Med*. 2001;46:24–30.
- Yang QX, Wang J, Zhang X, et al. Analysis of wave behavior in lossy dielectric samples at high field. *Magn Reson Med*. 2002;47:982–989.
- van de Moortele PF, Akgun C, Adriany G, et al. B1 destructive interferences and spatial phase patterns at 7 T with a head transceiver array coil. *Magn Reson Med*. 2005;54:1503–1518.
- Yarnykh VL. Actual flip-angle imaging in the pulsed steady state: a method for rapid three-dimensional mapping of the transmitted radiofrequency field. *Magn Reson Med*. 2007;57:192–200.
- Chung S, Kim D, Breton E, Axel L. Rapid B_1^+ mapping using a preconditioning RF pulse with turboFLASH readout. *Magn Reson Med*. 2010;64:439–446.
- Nehrke K, Börner P. DREAM—a novel approach for robust, ultrafast, multislice B1 mapping. *Magn Reson Med*. 2012;68:1517–1526.
- Sacolick LI, Wiesinger F, Hancu I, Vogel MW. B1 mapping by Bloch-Siegert shift. *Magn Reson Med*. 2010;63:1315–1322.
- Pohmann R, Scheffler K. A theoretical and experimental comparison of different techniques for B1 mapping at very high fields. *NMR Biomed*. 2013;26:265–275.
- Brunheim S, Gratz M, Johst S, et al. Fast and accurate multi-channel mapping based on the TIAMO technique for 7T UHF body MRI. *Magn Reson Med*. 2018;79:2652–2664.
- Dietrich S, Aigner CS, Kolbitsch C, et al. 3D free-breathing multichannel absolute B_1^+ mapping in the human body at 7T. *Magn Reson Med*. 2021;85:2552–2567.
- Ma D, Gulani V, Seiberlich N, et al. Magnetic resonance fingerprinting. *Nature*. 2013;495:187–192.
- Chen Y, Jiang Y, Pahwa S, et al. MR fingerprinting for rapid quantitative abdominal imaging. *Radiology*. 2016;279:278–286.
- Ma D, Coppo S, Chen Y, et al. Slice profile and B1 corrections in 2D magnetic resonance fingerprinting. *Magn Reson Med*. 2017;78:1781–1789.
- Cloos MA, Knoll F, Zhao T, et al. Multiparametric imaging with heterogeneous radiofrequency fields. *Nat Commun*. 2016;7:1–10.
- Lee Y, Callaghan MF, Nagy Z. Analysis of the precision of variable Flip angle T1 mapping with emphasis on the noise Propagated from RF transmit field maps. *Front Neurosci*. 2017;11:106.
- Buonincontri G, Sawiak SJ. MR fingerprinting with simultaneous B1 estimation. *Magn Reson Med*. 2016;76:1127–1135.
- Buonincontri G, Schulte RF, Cosottini M, Tosetti M. Spiral MR fingerprinting at 7 T with simultaneous B1 estimation. *Magn Reson Imaging*. 2017;41:1–6.
- Körzdörfer G, Jiang Y, Speier P, et al. Magnetic resonance field fingerprinting. *Magn Reson Med*. 2019;81:2347–2359.
- Cloos MA, Paška J, Yu Z, et al. Abdominal imaging with heterogeneous radiofrequency fields at 7 tesla. In Proceedings of the 25th Annual Meeting of ISMRM, Honolulu, HI; 2017:1125.
- van Riel MHC, Yu Z, Hodono S, et al. Free-breathing abdominal T1 mapping using an optimized MR fingerprinting sequence. *NMR Biomed*. 2021;34:e4531.

26. Cunningham CH, Pauly JM, Nayak KS. Saturated double-angle method for rapid B_1^+ mapping. *Magn Reson Med*. 2006;55:1326-1333.
27. Akoka S, Franconi F, Seguin F, Le Pape A. Radiofrequency map of an NMR coil by imaging. *Magn Reson Imaging*. 1993;11:437-441.
28. Flassbeck S, Schmidt S, Bachert P, Ladd ME, Schmitter S. Flow MR fingerprinting. *Magn Reson Med*. 2019;81:2536-2550.
29. Lin W, Song HK. Improved signal spoiling in fast radial gradient-echo imaging: applied to accurate T_1 mapping and flip angle correction. *Magn Reson Med*. 2009;62:1185-1194.
30. Jiang Y, Ma D, Seiberlich N, Gulani V, Griswold MA. MR fingerprinting using fast imaging with steady state precession (FISP) with spiral readout. *Magn Reson Med*. 2015;74:1621-1631.
31. Epstein FH, Mugler JP III, Brookeman JR. Spoiling of transverse magnetization in gradient-echo (GRE) imaging during the approach to steady state. *Magn Reson Med*. 1996;35:237-245.
32. Cao X, Ye H, Liao C, Li Q, He H, Zhong J. Fast 3D brain MR fingerprinting based on multi-axis spiral projection trajectory. *Magn Reson Med*. 2019;82:289-301.
33. Barnett AH, Magland JF, Klinteberg L a. A parallel non-uniform fast Fourier transform library based on an "exponential of semi-circle" kernel. *SIAM J Sci Comput*. 2019;41:C479-C504.
34. Barnett AH. Aliasing error of the exp ($\beta_1 - z_2$) kernel in the nonuniform fast Fourier transform. *Appl Comput Harmon Anal*. 2021;51:1-16.
35. Lerski RA, McRobbie DW, Straughan K, Walker PM, De Certaines JD, Bernard AM. Multi-center trial with protocols and prototype test objects for the assessment of MRI equipment. *Magn Reson Imaging*. 1988;6:201-214.
36. Seifert F, Wübbeler G, Junge S, Ittermann B, Rinneberg H. Patient safety concept for multichannel transmit coils. *J Magn Reson Imaging*. 2007;26:1315-1321.
37. Schoen N, Seifert F, Petzold J, et al. The impact of respiratory motion on electromagnetic fields and specific absorption rate in cardiac imaging at 7T. *Magn Reson Med*. 2022;88:2645-2661.
38. Gajdošík M, Chmelík M, Just-Kukurová I, et al. In vivo relaxation behavior of liver compounds at 7 tesla, measured by single-voxel proton MR spectroscopy. *J Magn Reson Imaging*. 2014;40:1365-1374.
39. Homann H, Börner P, Eggers H, Nehrke K, Dössel O, Graesslin I. Toward individualized SAR models and in vivo validation. *Magn Reson Med*. 2011;66:1767-1776.
40. Gavazzi S, van den Berg CAT, Sbrizzi A, et al. Accuracy and precision of electrical permittivity mapping at 3T: the impact of three B_1^+ mapping techniques. *Magn Reson Med*. 2019;81:3628-3642.
41. Lutz M, Aigner CS, Flassbeck S, et al. MRF-based channel-wise absolute B_1^+ mapping at low RF power in the human abdomen at 7T. Proceedings of the 31st Annual Meeting of ISMRM, Toronto, Canada; 2023:1420.
42. de Buck MHS, Kent JL, Jezzard P, Hess AT. Head-and-neck multichannel B_1^+ mapping and RF shimming of the carotid arteries using a 7T parallel-transmit head coil. *Magn Reson Med*. 2024;91:190-204.
43. Dietrich S, Aigner CS, Mayer J, et al. Motion-compensated fat-water imaging for 3D cardiac MRI at ultra-high fields. *Magn Reson Med*. 2022;87:2621-2636.
44. Block KT, Chandarana H, Milla S, et al. Towards routine clinical use of radial stack-of-stars 3D gradient-Echo sequences for reducing motion sensitivity. *J Korean Soc Magn Reson Med*. 2014;18:87-106.
45. Zhao B, Halder JP, Liao C, et al. Optimal experiment design for magnetic resonance fingerprinting: Cramér-rao bound meets spin dynamics. *IEEE Trans Med Imaging*. 2019;38:844-861.
46. Jordan SP, Hu S, Rozada I, et al. Automated design of pulse sequences for magnetic resonance fingerprinting using physics-inspired optimization. *Proc Natl Acad Sci*. 2021;118:e2020516118.
47. Cohen O, Rosen MS. Algorithm comparison for schedule optimization in MR fingerprinting. *Magn Reson Imaging*. 2017;41:15-21.
48. Vannesjo SJ, Haerberlin M, Kasper L, et al. Gradient system characterization by impulse response measurements with a dynamic field camera. *Magn Reson Med*. 2013;69:583-593.

SUPPORTING INFORMATION

Additional supporting information may be found in the online version of the article at the publisher's website.

Figure S1. Results of the pick-up loop experiments with the commercial head coil (Head Coil 1Tx/32Rx, Nova Medical, Wilmington, MA, USA). (A) Longer rise times ($\sim 100 \mu\text{s}$) and phase variations ($\sim 10^\circ$) were observed during the application of rectangular pulses in the A32 mode of the coil, which uses a separate 32-channel receive array. This effect was not observed in the V32 mode of the coil, where the transmit (Tx) birdcage coil is also used for signal reception and therefore that mode is used in this work, but worse SNR is expected at the edges of the phantom. We speculate that this effect is related to the switching circuitry of the Tx birdcage coil. (B) The RF pulses of the MR fingerprinting (MRF) FA train were sparsely sampled (every 10th pulse) and the sum over the positive main lobe was calculated for each pulse. This was then fitted with a constant scaling factor to the nominal MRF FA pattern and $\Delta\text{Amplitude}$ is the relative deviation from the measured to the nominal FA pattern. Two effects are observed: (i) an overall 2.5% increase in RF amplitude is observed from left to right, resulting in 2.5% higher FAs from cycle 3 onwards. Cycle 1 is the dummy cycle that is not used in the reconstruction, therefore the B1-MRF maps were corrected by this factor for the phantom experiments; (ii) Within a single cycle, differences of up to -11.4% are measured for low FAs while positive differences up to 1.8% are observed for high FAs. Initial attempts to correct the FA pattern of the MRF dictionary by the measurements of effect (ii) resulted in a reduced dot product for fully sampled B1-MRF scans (233 cycles), indicating a less accurate match between the measurements and the MRF dictionary. This observation suggests potential biases in the pickup loop experiments, such as reduced oscilloscope sensitivity at lower voltages or the effects of filtering.

Figure S2. Normalized Cramér–Rao bound (nCRB) in multiples of the variance of the Gaussian noise (σ^2). Higher nCRB values correspond to a higher lower bound on the variance of a parameter estimate and thus to lower sensitivity (Supplementary Information Note S2). The plots in (A) and (B) can be compared as both show normalized variants of the CRB. In general, large $\text{nCRB}/\sigma^2 > 105$ are observed for $T_1 > 400$ ms for all α_{\max} (Figure 2A) and thus low T_1 sensitivity. For $\alpha_{\max} = 4^\circ$, smaller nCRB/σ^2 values < 61 are observed for all T_1 (Figure 2B), indicating relatively high sensitivity to α_{\max} . Sensitivity to α_{\max} increases with decreasing T_1 and local maxima appear for $T_1 = 1300$ ms at $\alpha_{\max} = 15^\circ$ and for $T_1 = 2100$ ms at $\alpha_{\max} = 24^\circ$. For $\alpha_{\max} > 30^\circ$ the nCRB appears almost constant and $\text{nCRB}/\sigma^2 < 13$ for all T_1 values.

Figure S3. Influence of linear ΔB_0 variations of 0 Hz, 10 Hz, ... 100 Hz along the slice direction for $T_1 = 1300$ ms. For linear variations below 50 Hz, i.e., a range from -25 Hz to $+25$ Hz across the nominal slice thickness, no changes are visible in the signal curves. For 100 Hz variations can be observed from time frame 500 on in the $\alpha_{\max} = 60^\circ$ signal. For 50 Hz the mean signal deviation is 0.01%, 0.05%, 0.21%, 1.43% for $\alpha_{\max} = 5^\circ, 10^\circ, 20^\circ, 60^\circ$, respectively, compared to 0 Hz.

Figure S4. Dynamic range evaluation of B1-MRF, sat-TFL, AFI, BSS. Data similar to Figure 4E–H. However, instead of absolute errors, relative errors are shown, and the y-axis shows the maximum of the mean \pm std. Values up to 170° are shown compared to 100° in Figure 4 to cover the full dynamic range of the references. The dashed gray line indicates the error limit of $\epsilon = 10\%$ that was used for the dynamic range evaluation, where a dynamic range of 12.3 (6° – 74°) is observed for B1-MRF (A) and 5.0 (27° – 136°)/ 4.6 (39° – 180°)/ 3.3 (36° – 120°) for satTFL/AFI/BSS, respectively.

Figure S5. Comparison of the 1Rx (V32) and the 32Rx (A32) modes for a (2×2) mm² resolution with different number of cycles in the phantom. For B1-MRF, the ramping effect observed in the rectangular pulses is not noticeable because sinc pulses with a duration of 1 ms are used, where only small RF amplitudes occur in the first 100 μ s and little influence is expected. However, the 1Rx mode shows discontinuities in individual pixels for 5 cycles, mostly at the edge of the phantom, which do not appear in the 32Rx mode. This is due to the lower SNR of the birdcage coil (V32) at the edge of the phantom compared to the 32 array receive mode (A32).

Figure S6. Influence of T_1 on the \hat{B}_1^+ maps. (A) The first row shows the T_1 and \hat{B}_1^+ map of B1-MRF for volunteer 1. No reference was obtained for T_1 , but in regions of higher \hat{B}_1^+ amplitude ($> 2 \mu\text{T}/\sqrt{\text{kW}}$) the T_1 of B1-MRF of about 1000 ms (T_1 of water peak of liver tissue at 7 T in

a spectroscopy study 1362 ms) seems plausible. However, in regions with lower \hat{B}_1^+ ($< 2 \mu\text{T}/\sqrt{\text{kW}}$) amplitudes, large T_1 values are observed that are not expected physiologically. To investigate the effect of a mismatched T_1 , the second row shows the resulting \hat{B}_1^+ maps when only one $T_1 = 1368.1$ ms is used in the MRF dictionary. To quantify the difference on the \hat{B}_1^+ maps with only one T_1 compared to the full dictionary, the same mask is applied over the whole liver as for the Bland–Altman in Figure 8. A mean offset of $-0.02 \mu\text{T}/\sqrt{\text{kW}}$, is observed between the full dictionary and T_1 of 1368 ms. In percentage terms, this results in an average bias of -1.5% for the \hat{B}_1^+ map when each pixel is considered separately (overestimation of \hat{B}_1^+ due to T_1 mismatch). Thus, using the T_1 values from the spectroscopic study as ground truth ($T_1 = 1362$ ms) for liver tissue, an average overestimation of 1.5% in \hat{B}_1^+ is expected for mismatched T_1 . To investigate the effect of a mismatched T_1 on the \hat{B}_1^+ value over a wider T_1 range, a simulation study is shown (B) where the fingerprint of $T_1 = 1368.1$ ms (liver tissue) was matched to different dictionaries containing only one T_1 value. The T_1 difference to $T_1 = 1368.1$ ms is then considered as the T_1 error and is displayed in % on the x-axis. The y-axis shows the deviation in % for different \hat{B}_1^+ values. Experimental results (A) and CRB analysis (Supporting Information Figure S2) indicate that T_1 is less accurately quantified at lower \hat{B}_1^+ magnitudes ($\leq 1.5 \mu\text{T}/\sqrt{\text{kW}}$), which increases the likelihood of incorrect T_1 determination in this range. Nevertheless, errors in T_1 estimation for low \hat{B}_1^+ magnitudes result in relatively moderate \hat{B}_1^+ errors of up to 4.1% for \hat{B}_1^+ magnitudes $\leq 1.5 \mu\text{T}/\sqrt{\text{kW}}$. Conversely, at higher \hat{B}_1^+ magnitudes, such as $4 \mu\text{T}/\sqrt{\text{kW}}$ a maximum \hat{B}_1^+ error of -8.1% is observed at a T_1 error of -50% . However, at these elevated \hat{B}_1^+ magnitudes, T_1 is quantified with greater accuracy (A), thereby minimizing the potential for significant T_1 -related errors.

Figure S7. Statistical metrics of \hat{B}_1^+ over the liver. The same mask as in Figure 8 was applied. (A) shows box-plots, where the orange line shows the median and the box shows the interquartile range (IQR). The whiskers extend to $1.5 \times$ the IQR range from the box. Outliers are marked as circles. Differences between the distributions were evaluated statistically by a Mann–Whitney U test. Statistically significant results ($p < 0.05$) are denoted by a star (*) and not statistically significant results are denoted by “NS.” Mean, standard deviation and IQR for all volunteers are stated in (B).

Figure S8. Total differential (sum of partial gradients: $d\hat{B}_1^+ = \partial\hat{B}_1^+/\partial x \cdot \Delta x + \partial\hat{B}_1^+/\partial y \cdot \Delta y$) for the different methods for all volunteers. Focusing on the liver, discontinuities can be observed in low FA areas of satTFL and RPE-AFI for volunteer 2 and 3, which are not expected for the usually smooth B_1 fields.

Figure S9. Frequency response (B) of the pulses for the different methods for the in vivo scan where 90° FA is achieved at 0 Hz (A). The red dotted line in (B) marks the -1000 Hz off-resonance that is expected for the main fat peak at 7 T. Here, a deviation from 0 Hz of 8%, 96%, and 21% is observed for the sinc pulse (TBW4, 1.3 ms) (B1-MRF), a rectangular pulse of 1 ms (satTFL), and 0.5 ms (RPE-AFI), respectively. The gray shaded area marks the ± 400 Hz region where the water signal is expected due to ΔB_0 inhomogeneities. Here, the deviation is $<0.15\%$, $<10.31\%$, $<0.85\%$ for the sinc pulse (TBW4, 1.3 ms) (B1-MRF), a rectangular pulse of 1 ms (satTFL), and 0.5 ms (RPE-AFI), respectively.

Note S1. PEX Reconstruction.

Note S2. MRF Sensitivity Cramér-Rao Bound Analysis.

How to cite this article: Lutz M, Aigner CS, Flassbeck S, et al. B1-MRF: Large dynamic range MRF-based absolute B_1^+ mapping in the human body at 7T. *Magn Reson Med*. 2024;92:2473-2490. doi: 10.1002/mrm.30242